How good is dust emission as a tracer of star forming regions in molecular clouds?

TOMAS JAMES
STUDENT ID: 1158976

Supervisor: Dr. P. C. Clark

April 22, 2016

Abstract

A data analysis pipeline to analyse synthetic Herschel images of early star forming regions to probe the dust emission characteristics of the data was written in the Python programming language. Initially a simple scenario of a spherical, isothermal molecular cloud at $T = 10K$ was simulated using RADMC-3D (Dullemond, Juhasz, Pohl, Sereshti, Shetty, Peters, Commercon, and Flock n.d.), with bespoke input files generated using the Python programming language. This simulation was performed across the 3 SPIRE (Griffin et al. 2010) wavebands centered on 250 μm, 350 μm and 500 μm as well as the 3 PACS (Poglitsch and Altieri 2009) wavebands centered on 72 μm, 103 μm and 167 μm. This data was then 'degraded' by accounting for the instrument's transmission curve to better simulate an object observed by Herschel. This data was then subsequently analysed by plotting Spectral Energy Distributions (SEDs) on a pixel by pixel basis where the goodness-of-fit was assessed using a χ^2 test. This routine allowed recovery of the column density N and temperature T at each pixel. These values were then used to produce 2-dimensional maps of these regions, subsequently being compared to the 2-dimensional produces from the initial input data. of density and temperature. Finally this machinery was applied to data from the SPH simulation Arepo in order to simulate observations of molecular clouds in Herschel. It was found that the dust properties recovered using the χ^2 test were of the correct range however the observed biases stated in Shetty, Kauffmann, Schnee, Goodman, and Ercolano (2009), Shetty, Kauffmann, Schnee, and Goodman (2009) and Kelly et al. (2012) were evident such that the χ^2 test underestimated values of T at lower temperatures and overestimated values of T at higher temperatures. As Shetty, Kauffmann, Schnee, Goodman, and Ercolano (2009) states this is a result of the line of sight temperature variations.

Contents

List of Figures

List of Tables

Chapter 1

Introduction

1.1. MOLECULAR CLOUDS

A molecular cloud is a dense region of the Interstellar Medium (ISM), composed primarily of molecular Hydrogren (H_2) at temperatures $< 20\ K$ (Hildebrand 1983). Despite the cloud being primarily a gas of H_2, a small (by mass) dust component is also present. This dust mass component is approximately 1% the gas mass according to Shetty, Kauffmann, Schnee, Goodman, and Ercolano (2009), however despite this minimal presense dust remains a crucial component in the evolution of the cloud and the subsequent star forming process.
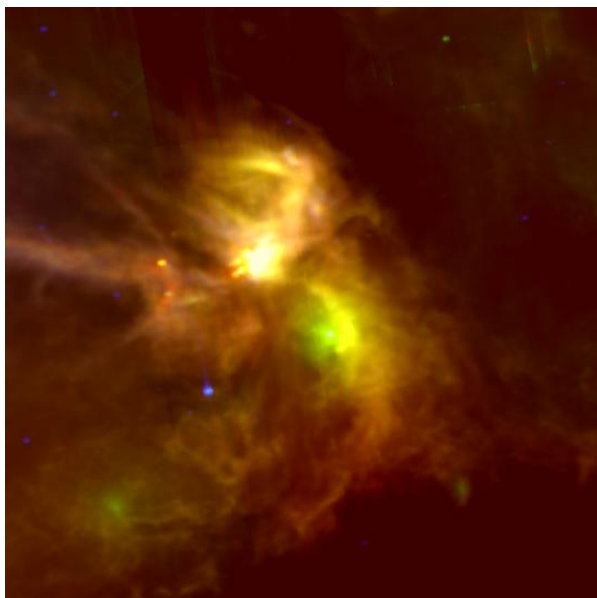

Figure 1.1: *An IRAS image showing the Rho Opiuchi cloud complex (Caltech n.d.).*

Figure 1.1 shows the Rho Ophiuchi cloud complex as imaged by the Infra-red Astronomical Satellite (IRAS). Rho Opiuchi is the nearest active star forming molecular cloud complex to the Milky Way[1]. As a result of this, Rho Ophiuchi provides an unprecedented oppurtunity to study the sites of early star formation at high resolution. This is in spite of the large uncertainty in estimates of the distance to Rho Ophiuchi (Mamajek 2008).

Much like the ISM, molecular clouds are composed of gas and cosmic dust, however a molecular cloud differs from the ISM in that significantly greater densities are found within a molecular cloud than that of the ISM. The dust density in a molecular cloud is thought to be around $10^5\ g\ cm^{-3}$, whilst the dust density in the surrounding ISM is thought to be around $10^2\ g\ cm^{-3}$.

The molecular cloud is also colder than the surrounding ISM: the temperature is approximately 15 K in the ISM whilst the temperature in the molecular cloud is approximately 10 K. The warmer ISM bathes the cooler cloud, resulting in a temperature gradient; the ISM heats the cloud from the outside in, resulting in a temperature that increases with distance from the centre of the cloud.

Figure 1.1 illustrates the intense infra-red emission within molecular clouds owing to the active star forming occurring within them. It also illustrates the turbulence and chaos within the cloud, with both filamentary structure and (potentially) magnetic fields running through the cloud itself. These filaments are regions of higher density, and as Larson (1994) states "One fundamental characteristic of molecular clouds is that they are not, as has sometimes been assumed, isolated billiard balls moving about independently in space, but instead are just dense condensations in more widely distributed, mostly atomic gas. Although molecular clouds may often appear to have sharp boundaries, these boundaries do not represent the edge of the matter distribution but just rapid transitions from the molecular gas to the surrounding atomic gas, which is distributed in extended envelopes that typically have comparable mass (Blitz 1988, 1991)". These filaments act as preferential sites for star formation (Murphy and von Schill 2014).

---

[1]Mamajek (2008) estimates the range of distances as being between 125pc-165pc - a range of almost 40%.

1.1.1. Star forming conditions

These star forming regions within molecular clouds originate from locations of gravitational instability that lead to subsequent collapse (Jeans 1902). A stable cloud (or portion of a cloud) is in hydrostatic equilibrium, such that the force due to gravity is balanced by the force due to gaseous pressure from the gas within the cloud. This equilibrium state can also be regarded as a virialised state such that $2K + U = 0$, where K is the total kinetic energy of the system and U is the total potential energy of the system. The cloud begins to collapse when the gravitational force is greater than the force due to the hydrostatic pressure. This collapse continues unimpinged until such a time that another opposing force can halt the collapse. The initial collapse is triggered when a region within the molecular cloud has a mass that exceeds the Jeans' mass given by Equation 1.1 (Pettini 2011). This is known as the Jeans Criterion.

$$M_J = \left(\frac{5kT}{GM}\right)^{\frac{3}{2}} \left(\frac{3}{4\pi\rho}\right)^{\frac{1}{2}} \tag{1.1}$$

Within Equation 1.1, k is the Stefan-Boltzmann constant, T is the temperature of the region, G is the Universal Gravitational Constant, M is the mass of Hydrogen in the region and ρ is the density of the region prior to collapse. The collapse of an M_J mass region occurs according to the free-fall time, t_{ff} described in Equation 1.2 (Krumholz 2011).

$$t_{ff} = \sqrt{\frac{3\pi}{32G\rho}} \tag{1.2}$$

Variables within Equation 1.2 are as they were defined in Equation 1.1.

Interestingly the onset of collapse is also the onset of gravitational binding. According to Dobbs, Burkert, and Pringle (2011), the majority of a molecular cloud remains gravitationally unbound, further reinforcing the idea stated in Larson (1994) that molecular clouds are diffuse, transiest structures. The onset of gravitational binding is also not a singular process. A region of a molecular cloud may begin to collapse under the Jeans' criterion in Equation 1.1, however this clump may then sub-fragment into smaller clumps that also begin collapsing in a similar manner.

1.2. Dust emission

Dust is a relatively small fraction of the total ISM mass, estimated as being only 1% according to Shetty, Kauffmann, Schnee, Goodman, and Ercolano (2009). Whilst the dust mass accounts for such a small mass component, it still presents an important role in forming stars. The sources of flux embedded deep within the cloud radiate across a wide range of wavelengths, however the dust surrounding the source has the effect of absorbing and then re-radiating photons at a different wavelength. As such, these sources of flux (be they prestellar cores, protostars or pre-main sequence stars) are occluded by the dust enveloping them.

According to Shetty, Kauffmann, Schnee, Goodman, and Ercolano (2009), dust radiates as a modified black body in the far infra-red regime (i.e. from $\lambda = 60\,\mu m$) that can approximated using Equation 1.3.

$$S_\nu = N\Omega\kappa_0 \left(\frac{\nu}{\nu_0}\right)^\beta B_\nu(T) \tag{1.3}$$

In Equation 1.3 S_ν is the flux density, N is the column density, Ω is the solid angle subtended by the beam, κ_0 is a reference dust opacity, ν is the frequency of the image, ν_0 is a reference frequency at which the reference opacity κ_0 was evaluated at, β is the dust spectral index (for siliciate and carbonaceous grains, Draine and Lee (1984) approximates $\beta \sim 2$) and $B_\nu(T)$ is the frequency dependent Planck function. An assumption made here, as stated by Kelly et al. (2012), is that the dust is optically thin such that $\tau_\nu = N\kappa_\nu \ll 1$. The term $\kappa_0(\frac{\nu}{\nu_0})^\beta$ is the Hildebrand dust opacity law κ_ν given in Hildebrand (1983). In terms of intensity this equation becomes:

$$I_\nu = \frac{N}{R_{dust-gas}} \mu m_p \kappa_0 \left(\frac{\nu}{\nu_0}\right)^\beta B_\nu(T) \tag{1.4}$$

All variables in Equation 1.4 are as defined in Equation 1.3, with the addition of $R_{dust-gas}$. $R_{dust-gas}$ is the dust-to-gas ratio, here approximated as being 100. Throughout this project, dust emission was quantified in terms of intensity rather than flux density, as intensity is independent of distance to the source of emission.

Dust properties such as the spectral index β, temperature T and column density N clearly have an effect on dust emission according to Equations 1.3 and 1.4. Importantly, both Equations 1.3 and 1.4 describe dust emission at a single temperature T. This is illustrated in Figure 1.2. These properties, however, are experimentally difficult to measure and Kelly et al. (2012) states that most observational attempts to determine T and β rely on a χ^2 SED fitting routine. This routine does, however, suffer from drawbacks that make in unreliable in certain conditions.
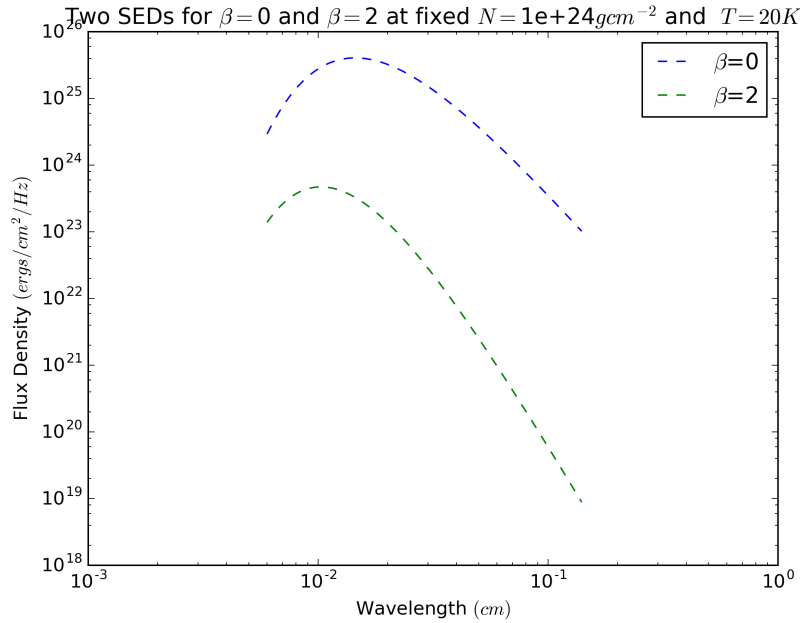
Figure 1.2: *A plot illustrating how the dust spectral index β varies the emergent dust SED whilst both N and T remain fixed. This is based off of a plot found in Shetty, Kauffmann, Schnee, Goodman, and Ercolano (2009).*

1.2.1.   The β-T degeneracy

As Equation 1.4 shows, dust does not radiate as a perfect blackbody. This is accounted for by multiplying the Planck function (i.e. the function that describes a body that radiates as a perfect blackbody) by the dust opacity term $\kappa = \kappa_0 (\frac{\nu}{\nu_0})^{\beta}$. Two key variables here are the dust spectral index β and the dust temperature T. These two properties suffer from a degeneracy (Keene et al. 1980) such that any χ^2 test applied to determining the values of β and T may understimate one parameter whilst overestimating another.

As Shetty, Kauffmann, Schnee, Goodman, and Ercolano (2009) states, a fitting routine for β and T is prone to overestimates owing to the assumption that temperature is constant along the line of sight. For an isothermal source this assumption may be well placed however in the case of a complex structure such as a molecular cloud shown in Figure 1.1 this assumption is inaccurate. Equations 1.3 and 1.4 describe dust emission from an isothermal source, i.e. one in which the dust is at one discrete temperature. Molecular clouds are not isothermal and have a range of temperatures along the line of sight, and as Shetty, Kauffmann, Schnee, Goodman, and Ercolano (2009) highlights, the SEDs describing the dust emission in these instances are actually combinations of the individual SEDs from each individual temperature source.

1.3. HERSCHEL SPACE OBSERVATORY

The Herschel Space Observatory was an ESA mission launched in 2009 with the primary objective of imaging cold regions of the Universe (Garcia-Lario et al. n.d.) and (ESA n.d.). Herschel had a number of objectives. As ESA (n.d.) states, these objectives included "targeted observations of star formation and both young and old stars, to reveal the physical and chemical processes in the early and later phases of a stars life." To achieve this, Herschel was launched with 3 different instruments on-board: Photodetector Array Camera and Spectrometer: PACS (Poglitsch and Altieri 2009), Spectral and Photometric Imaging Receiver: SPIRE (Griffin et al. 2010) and Heterodyne Instrument for the Far Infrared: HiFi (Helmich 2011). One of these instruments, SPIRE, was designed to probe the sites of early star formation deep within molecular clouds. This was achieved by imaging solely in the infra-red and sub-mm regimes. Herschel itself, across all instruments and functional modes, is sensitive to a range of wavelengths quoted by Garcia-Lario et al. (n.d.) as $\sim 55\,\mu\text{m}$ to $\sim 672\,\mu\text{m}$. Both PACS and SPIRE were capable of being run in "Parallel mode" - effective simultaneous operation according to Garcia-Lario et al. (n.d.). SPIRE itself had an photometry wavelength range $\sim 200\,\mu\text{m}$ to $\sim 670\,\mu\text{m}$ whilst PACS was sensitive to a photometry wavelength range $\sim 60\,\mu\text{m}$ to $\sim 210\,\mu\text{m}$. This therefore produces effectively continuous coverage of the wavelength range $\sim 60\,\mu\text{m}$ to $\sim 670\,\mu\text{m}$. [2]

Tables 1.1 and 1.2 illustrates the passbands for each of the filters within SPIRE and PACS.

Filter	Passband (μm)
PSW	199.4540 – 298.5657
PMW	281.6949 – 424.7548
PLW	391.4346 – 690.8139

Filter	Passband (μm)
Blue	55.6706 – 97.7403
Green	79.1026 – 135.1498
Red	117.7762 – 243.6431

Table 1.1: *The passbands (for extended source) for the SPIRE instrument (SVO Filter Profile Service n.d.).*   **Table 1.2:** *The passbands for the PACS instrument (SVO Filter Profile Service n.d.).*

In order to achieve the effective wavelength range described in Tables 1.1 and 1.2, both SPIRE and PACS detectors required extensive cooling to a temperature of $0.3K$ via ^3He sorption coolers (Garcia-Lario et al. n.d.). Again according to Garcia-Lario et al. (n.d.) the image focal plane required cooling to $1.7K$, again achieved using 2160 litres of Helium cryogen. To minimise any thermal radiation from the observatory itself, the spacecraft was radiatively cooled to a temperature of $85K$ (Garcia-Lario et al. n.d.). These temperatures allowed effective detection (via a bolometric detector in the case of SPIRE and a photometer in the case of PACS) of infra-red and sub-mm photons.

1.4. RADMC-3D

RADMC-3D is a 3-dimensional Monte-Carlo radiative transfer and ray tracing code developed by Cornelis Dullemond and written in Fortran 90 for radiative transfer and emission astrophysics in dusty environments (Dullemond, Juhasz, Pohl, Sereshti, Shetty, Peters, Commercon, and Flock n.d.).

RADMC-3D is able to compute dust emission intensity as well as Spectral Energy Distributions (SED) and spectra for a number of different continua. This project focussed only on dust continuum, neglecting gas. The dust emission intensity can be computed using 2 different methods: the thermal Monte-Carlo simulation, or an image ray trace. All computations require input files for RADMC-3D to read and use in its simulations. RADMC-3D 's Python port, `radmc3dPy` (Juhasz n.d.), is able to write these input files, however for this project a custom script was written such that file creation was independent of `radmc3dPy`.

1.4.1. `radmc3dPy`

Whilst RADMC-3D is written in Fortran 90, a Python wrapper, `radmc3dPy` allows Python to handle RADMC-3D objects.

---

[2]Further coverage is achieved down to 55 μm using HiFi however this is only achievable for spectroscopic applications.

1.4.2. Input files

As stated in Section 1.4, RADMC-3D requires a number of user defined input files in order to operate. These input files act as parameter spaces, defining boundary conditions along with step sizes for each given input files. Figure **??** shows a workflow of RADMC-3D's operation, including all files required in order to operate.
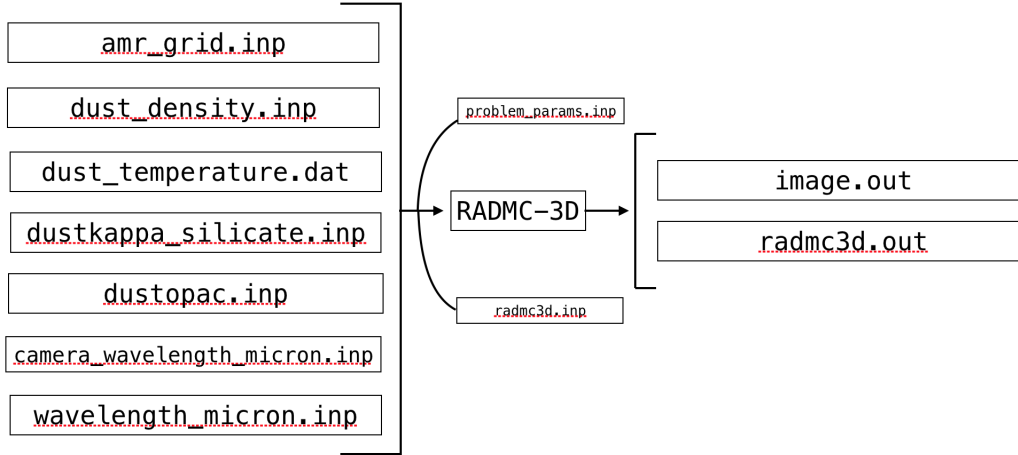
Figure 1.3: *A schematic representation of the RADMC-3D workflow.*

As Figure 1.3 illustrates, all input files to RADMC-3D have extension `.inp` whilst all output files have extension `.out`. Any intermediate files, such as those directly calculated by RADMC-3D, have extension `.dat`. *Most* input files' initial lines - the header information - contain quantitative information regarding the number of pixels/cells in the file, the pixel/cell width along with other identifiers that inform RADMC-3D whether to look for binary files, the number of dust species being considered as well as the number of datapoints in the file.

`amr_grid.inp` is the file used in order to create a spatial domain within the model. It does this by defining the start and end points of pixels in 3 dimensions: x, y and z. These definitions produce pixels, each of fixed width defined by the distance between pixel start and end points. RADMC-3D also has the ability to perform Adaptive Mesh Refinement, such that regions of interest can be split into more pixels (and have a smaller pixel width and therefore simulated higher resolutions) than, for example, regions of the ISM that do not require a higher resolution. Any further files that setup physical quantities draw directly from the structure of `amr_grid.inp`. They essentially 'insert 'a value of a physical quantity into each cell, therefore producing another parameter space. This structure is illustrated in Figure 1.4.2.

The index of each cell in Figure 1.4.2 is that cell's position in `amr_grid.inp`. For example,

`dust_density.inp` is the file that gives RADMC-3D its density information. It has the same structure as `amr_grid.inp`, however in place of the start

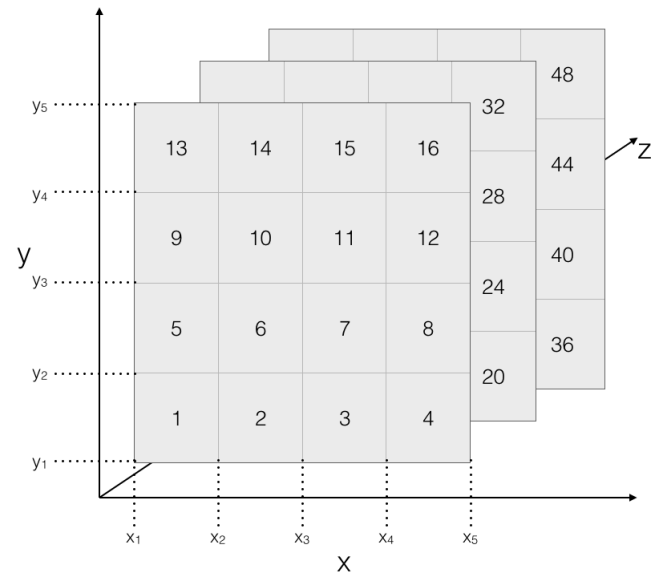**Figure 1.4:** *A pictorial representation of the structure of* `amr_grid.inp` *for a 4x4x3 grid. The index of a cell, denoted by the number contained within it, is the position of that cell in* `amr_grid.inp`. *This image is based off of an image in Dullemond, Juhasz, Pohl, Sereshti, Shetty, Peters, Commercon, Flock, and Min (n.d.).*

and end pixel points that are found in `amr_grid.inp`, `dust_density.inp` defines the dust density (in *cgs* units) at each pixel. This therefore creates a density parameter space with which to work from. Similarly, `dust_temperature.dat` draws upon the same idea, however instead of defining dust densities, `dust_temperature.dat` defines the dust temperature (in *K*) at each pixel point. These 3 files therefore create 3 parameter spaces: spatial, density and temperature.

Another crucial file is the `wavelength_micron.inp` file. This input file defines the wavelengths over which RADMC-3D should compute. By default, `wavelength_micron.inp` runs from 0.1 μm to 1000 μm with 150 points. Dust emission intensity can then be determined at any wavelength between these two bounds. In reality however, computing dust emission intensity over such a wide wavelength range is not always necessary (or practical). RADMc-3D thus allows the user to define a `camera_wavelength_micron.inp` file. This file is designed to constrict the range of wavelengths over which RADMC-3D computes, thus emulating the wavelengths available to a given telescope or filter. In this project `camera_wavelength_micron.inp` was used in order to allow RADMC-3D to compute dust emission intensity in wavelength bands corresponding to those found on both SPIRE (Griffin et al. 2010) and PACS (Poglitsch and Altieri 2009).

1.4.3. Thermal Monte-Carlo dust emission

?? The thermal Monte-Carlo simulation is able to compute dust temperatures using the technique described in Bjorkman and Wood (2001) from user-defined dust densities, providing a source of flux (and therefore photons) exists. This source of flux can either be through a star in the image space or an Interstellar Radiation Field. The process used to compute the dust temperature, according to Dullemond, Juhasz, Pohl, Sereshti, Shetty, Peters, Commercon, Flock, and Min (n.d.), is as follows. The total luminosity of the source is first split into *nphot* photon packets. The code then proceeds to 'fire 'photons out from the flux source into the image space. These photons can then either scatter off of dust grains or be absorbed by one, thus immediately being re-emitted at a different wavelength and direction as defined in Bjorkman and Wood (2001). Under scattering/re-emission the photon will travel through the image space as defined in `amr_grid.inp` - see Section 1.4.2 - entering different adjoining pixels as it does so. This increases the temperature of that pixel, again according to Bjorkman and Wood (2001). This process of 'ping-ponging 'throughout the image space is continued until the photon packet leaves the image space. At this point, a new photon packet is 'fired 'and the process is repeated using the previously determined dust temperatures until no further photon packets remain. The dust temperature at this point is therefore the solution.

Naturally the more pixels an image space comprises then the longer the simulation takes to compute owing to the large number of pixels and therefore collisions encountered. Likewise the greater the dust density at a given point the longer the simulation takes to run owing to a similar effect. Normally, RADMC-3D would write the calculated dust temperatures to `dust_temperature.dat` however as the thermal Monte-Carlo simulation was not used in this project, RADMC-3D was supplied with idealised dust temperatures in the form of a pre-determined `dust_temperature.dat` file.

1.4.4. Ray tracing dust emission

?? Conversely the image ray trace reads in both user-defined dust temperatures and dust densities, thus bypassing the computation of the dust temperatures as would have been the case in the thermal Monte-Carlo simulation. Again, according to Dullemond, Juhasz, Pohl, Sereshti, Shetty, Peters, Commercon, Flock, and Min (n.d.), the ray-trace follows, by default, a first-order integration where the source function, $S = j_\nu/\alpha$ and opacity (and therefore extinction α) are constant across the ray. This is described by Equation 1.4.4.

$$I_{result} = I_{start}e^{-\tau} + (1 + e^{-\tau})S \tag{1.5}$$

I_{result} is the dust emission intensity of the cell, I_{start} is the dust emission intensity of the cell prior to the ray entering it and τ is the optical depth along the path of the ray through the cell. The optical depth τ is defined as $\tau = \alpha s$ where α is as

defined earlier and s is the distance the ray travels through the cell. The option to perform second-order integration is also made possible by varying the source function S and extinction across the ray. Specifically S and α are fixed at the ingress and egress points of the ray. These points act as boundary conditions such that the variation in S amd α can then be linearly interpolated across the path of the ray through the cell.

The result, however, is the same in both Thermal Monte-Carlo simulation and ray-trace: an `image.out` file that contains the dust emission intensity at each cell in the image plane. RADMc-3D is also capable of accounting for scattering of photons off of dust grains however this project focussed solely upon absorption and re-emission only.

Chapter 2

Methodology

2.1. MODEL SETUP

In order to begin developing analysis tools a "test-bed" was required. This test-bed comprised a simple, spherical cloud of uniform density and temperature placed within a medium of greater temperature and lower density. This effectively simulated a cold and dense molecular cloud bathed in a warmer, diffuse ISM. Prior to this however it was necessary to investigate the simulation software's (RADMC-3D) operation. This was achieved using example scripts bundled with the code.

2.1.1. Example scripts

RADMC-3D includes a number of basic example scripts to familiarise the user with the software's operation and capabilities. As a result, they provide an excellent introductory exercise to using RADMC-3D. Examples of 1D and 2D thermal Monte-Carlo simulations were run in this regard, generating Figures 2.1 and 2.2.
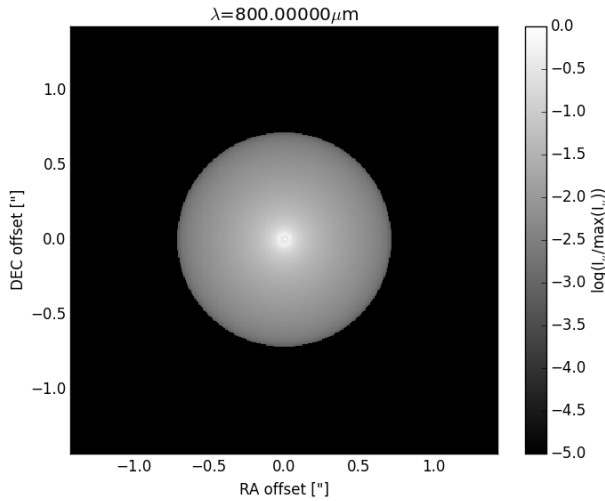

Figure 2.1: *The RADMC-3D output for dust emission intensity computed using thermal Monte-Carlo simulation in 1D.*
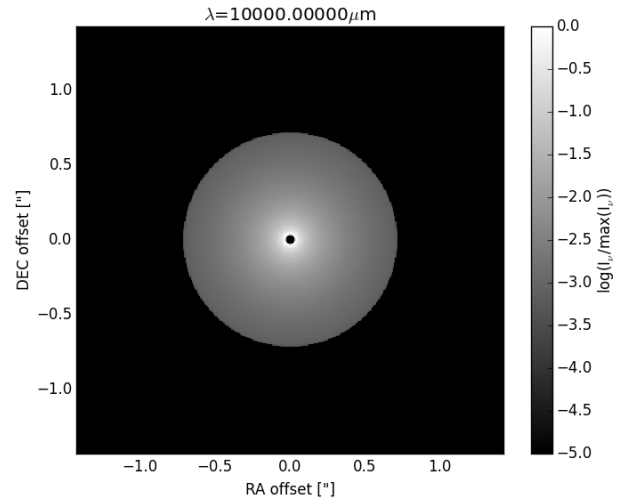
Figure 2.2: *The RADMC-3D output for dust emission intensity computed using thermal Monte-Carlo simulation in 2D.*

In order to begin operation, RADMC-3D's example scripts were analysed and run. The examples were used to understand how RADMC-3D generated the input files required (and as discussed in Section 1.4.2) as well as how the code used them and for what purpose. These examples were basic, consisting of both 1D and 2D sphere projections with user defined stars at their centres.

These examples ran thermal Monte-Carlo simulations. The first stage in this computation after writing the input files from the user inputs was to build dust temperatures. This was achieved using the process described in Section **??**. Once dust temperatures had been computed, RADMC-3D then performed a ray-trace in order to build the dust emission intensity. This was again achieved using the method described in Section **??**.

2.1.2. Modelling a cloud

To begin building 3D models outside of the example scripts, specific input files needed to be created. As stated, a custom Python script `datafilegen.py` was written to handle this file creation. Traditionally, `radmc3dPy` would handle file creation at the model setup phase, however given that RADMC-3D is designed to be run from the command line it was determined that reducing the number of dependencies would allow greater compatibility with different machines. This is critical if the code was to be run on a machine that may not have `radmc3dPy` installed, such as a supercomputer for larger computations. This also resulted in some of `radmc3dPy's` model setup commands being made redundant. For example, `radmc3dPy.setup.problemSetupDust` sets up the model using input parameters that are parsed to a model file. This phase was handled solely by `datafilegen.py`, so this command was redundant. Instead, required parameters such as the number of pixels in each dimension was given to RADMC-3D when calling it from the command line using `os.system(radmc3d image loadlambda)`. Again, the image ray-trace could be initiated through Python via the `os.system(radmc3d image)` command. The `loadlambda` keyword informs RADMC-3D that it should use the `camera_wavelength_micron.inp` module.

RADMC-3D then performs its raytrace using the method discussed in Section **??** and outputs the computed intensities to an `image.out` file. This image is a 2D image with image dimensions in the x-y plane corresponding to the initial x and y image dimensions supplied to RADMC-3D. This file contains the dust emission intensity values at each pixel within that plane. This intensity is, however, an idealised intensity that does not account for any ineffeciences. It was assumed that the source is imaged in the absence of any occluding material along the line of sight between the observer and the source, and thus exctinction was neglected.

By supplying `datafilegen.py` with the mass of the cloud, along with the number density of dust both inside and outside of the cloud, the code then calculates the expected radius of the cloud using a simple mass-density-volume relation. By then supplying the number of image dimensions ($128 \times 128 \times 128$) and the image bounds ($2r$ where r is the radius of the cloud) the spatial parameter space for `amr_grid.inp` can be computed. The density and temperature data is then assigned depending upon whether the pixel under consideration lies inside or outside of the idealised isothermal, spherical cloud.

It was necessary however in order to simulate data as imaged by Herschel to account for the frequency dependent transmission of Herschel's filters.

2.1.3. Simulating Herschel

No telescope or observatory can produce perfect images or data; components within the telescope, the observatory or the surroundings all degrade the data quality. In real world applications maximising the SNR is crucial to data quality, but the principles of this will not be touched on here. Furthermore SNR (and therefore integration time) is not accounted for in the simulations or data analysis - images are plotted as if the source is integrated for sufficient time such that the fictional "detector" responds and detects all photons from the source incident upon it as they were emitted from the dust.

Naturally this is an idealised assumption; not all photons that fall on a detector are detected. Detectors have a given responsivity that is a measure of how many of the incident photons contribute to the signal. Furthermore, filters are essential to telescope operation as they discriminate wanted and unwanted frequencies to ensure only frequencies within the passband of interest are transmitted to the detector. This introduces a large inefficiency in that not all incident photons are transmitted owing to reflection off of the filter itself, as well as absorption within the filter. This is frequency dependent and thus produces a "transmission curve".

2.1.4. Transmission

This transmission curve varies depending on the filter under consideration and therefore acts as a measure of characterisation. As SPIRE's PSW, PMW and PLW bands along with PACS' Blue, Green and Red filers were considered for this project their transmission data was required. This data was downloaded from SVO Filter Profile Service (n.d.) and subsequently plotted using Python. Figure 2.1.4 shows the transmission curves as a function of frequency for each band.
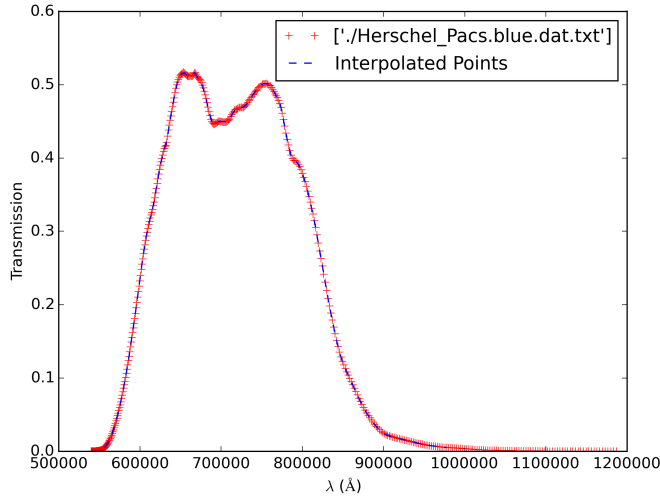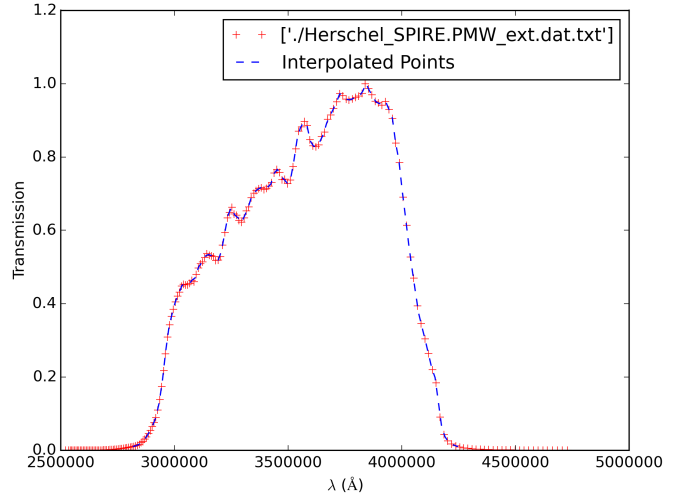
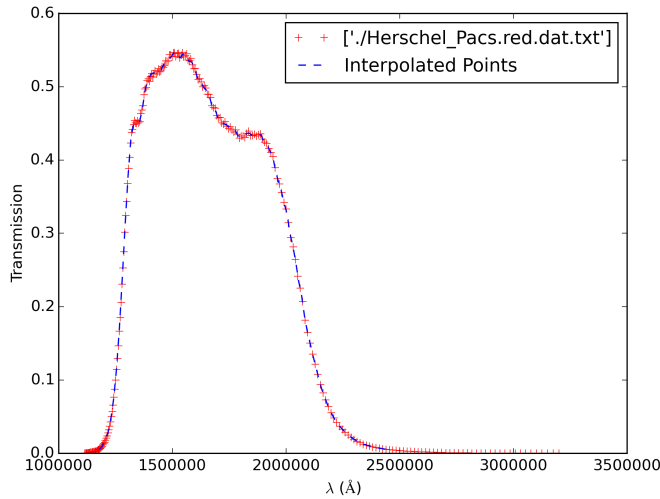**(a)** *The transmission curve for the PACS Blue band.*
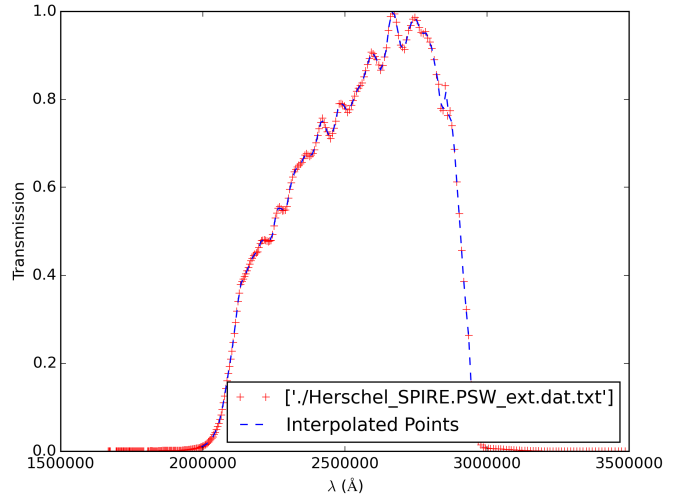
(b) *The transmission curve for the SPIRE PSW band.*
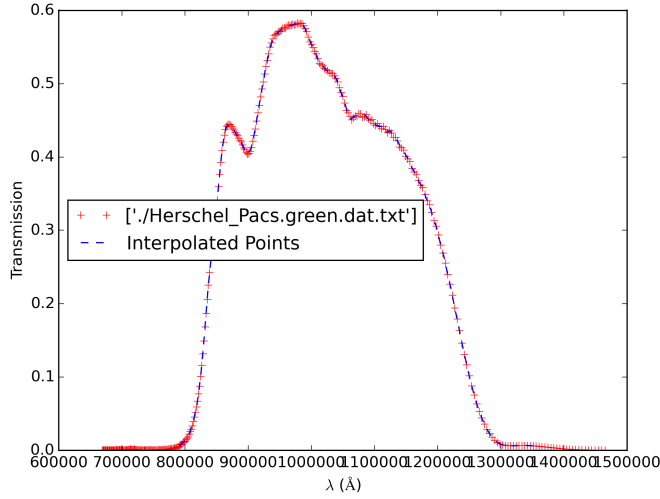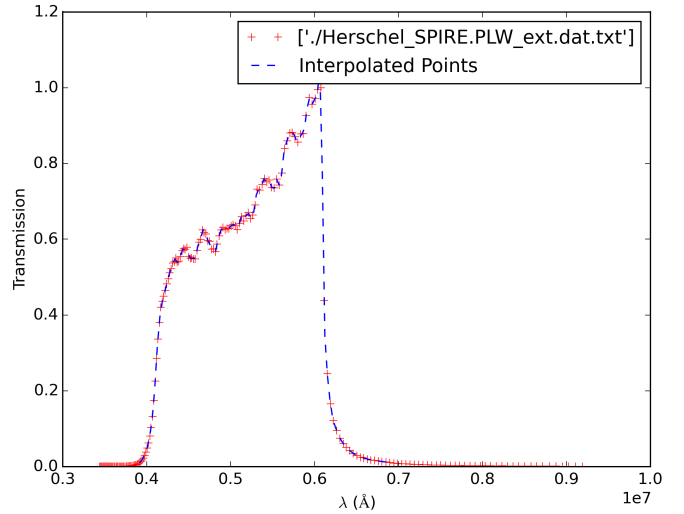

(c) *The transmission curve for the PACS Green band.*

(d) *The transmission curve for the SPIRE PMW band.*

(e) *The transmission curve for the PACS Red band.*

(f) *The transmission curve for the SPIRE PLW band.*

In order to begin accounting for the transmission effects it was necessary to multiply each datapoint at a given frequency/wavelength by the transmission coefficient at that frequency/wavelength. However the data downloaded from SVO Filter Profile Service (n.d.) did not have linearly spaced intervals, resulting in the transmission coefficients and freqencies supplied not matching with those used in the simulation (specifically the data in `camera_wavelength_micron.inp` file). To account for this, Python's `interp1d` function was used. This function would construct linearly spaced intermediate points between the existing datapoints supplied using a 'cubic' routine[1]. The result was a reconstruction of the original data with a user-defined number of points between upper and lower bounds. By choosing these upper and lower bounds to match the upper and lower bounds of `camera_wavelength_micron.inp` (with the same number of wavelength points) the transmission curve could be reconstructed to match the temporal data supplied to the simulation. Figure 2.1.4 illustrates this. The red $+$ datapoints indicate the original data supplied from SVO Filter Profile Service (n.d.), whilst the blue $--$ datapoints indicate the reconstructed, interpolated data. The interpolation is handled by `datafilegen.py` at the input file creation phase.

2.1.5. Composite imaging

In reality images are not taken at one discrete wavelength. Instead, images are a composite of wavelengths across a broad range defined by the telescope's filter. To illustrate, consider the SPIRE PSW band. As Table 1.1 illustrates, the PSW band is sensitive to wavelengths in the range $199.4540\,\mu m - -298.5657\,\mu m$. This means that an image using the PSW band is actually a composite image comprising a weighted average of the wavelengths imaged across such that the emergent image is effectively an image taken at the central band wavelength. As a result of this, any transmission effects had to be accounted for in the image composition, such that Equation 2.1.5 was used to construct the image intensities at each pixel.

$$I_{pix} = \frac{\sum_{i,j=0}^{xpix,ypix} I_{\nu_i} T_{\nu_i}}{\sum_{i=0}^{npix} T_{\nu_i}} \tag{2.1}$$

I_{pix} is the pixel intensity whilst I_{ν_i} and T_{ν_i} are the intensity and transmission coefficient at frequency ν_i respectively. By performing the product of the intensity across all considered frequencies (i.e. ν_i) at pixel $(xpix, ypix)$ with the transmission coefficent across all considered frequencies and normalising by dividing by the sum of all of the transmission coefficients in the dataset, the transmission weighted intensity can be computed at each pixel. Figure **??** illustrates the output for a 3-dimensional isothermal cloud in RADMC-3D with perfect transmission (i.e. no transmission convolution). Figure 2.5 illustrates the same image but with transmission being accounted for according to Equation 2.1.5. These images are computed in the Herschel PSW band.

2.2. ANALYSIS ROUTINE

2.2.1. Spectral energy distributions (SEDs)

Each individual source of flux has an energy distrubtion; that is, a function of how that point radiates as a function of frequency/wavelength. This function is continuous, and in the case of a blackbody source the SED can be described by the Planck function. Within the synthetic observations used in this project, each pixel within the computed image (rather than a discrete point) has an energy distribution. The SEDs in these cases are approximated using Equation 1.4 as opposed to the unaltered Planck function[2]. When imaging an object however this continuous SED is not observed. Instead, the telescope 'sees' one, discrete intensity for each resolved point owing to the telescope's averaging over all observed frequencies as discussed in Section 2.1.5. Figure 2.2.1 illustrates this.

Figure 2.2.1 shows the SED for the central pixel (0,0) of Figure 2.5 imaged in the PSW band. This SED is sampled directly from `image_trans.out` by taking the intensity of the pixel (in this case the (0,0) pixel) at each discrete frequency/wavelength considered. Plotting the intensity as a function of frequency produces the red continua in the left hand panel. Convolving the

---

[1]Other routines to interpolate were available, however the cubic routine provided accurate results so alternatives were not exploreed.
[2]Whilst the Planck function does not describe dust emission in this instance, a modified version of the Planck function does
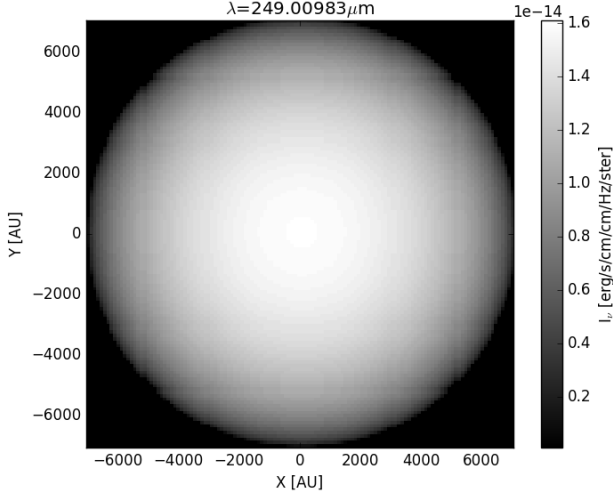
Figure 2.4: *The emergent image (before transmission effects) of a raytrace on a $1M_{Sun}$ spherical, 3D, isothermal ($T = 10K$) cloud.*
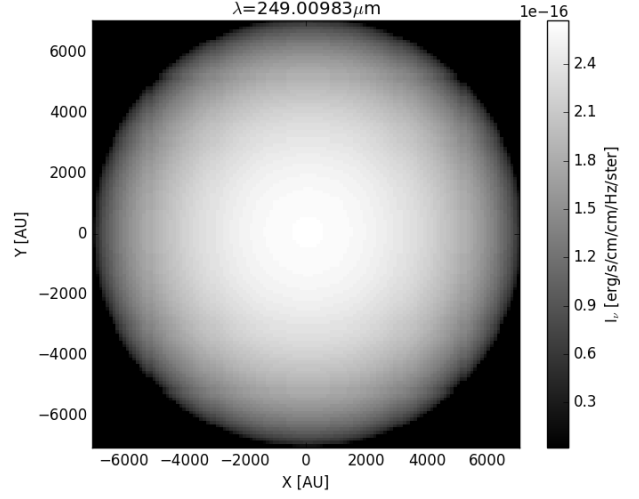

Figure 2.5: *The emergent image (after transmission effects) of a raytrace on a $1M_{Sun}$ spherical, 3D, isothermal ($T = 10K$) cloud.*

theoretical SED with the transmission curve for the band imaged in produces the SED that falls on to Herschel's filter. This is displayed as the blue curve in the left hand panel. The green point represents the intensity 'seen' by Herschel, as determined by Equation 2.2.1.

$$I_s = \frac{\sum_\nu I_{pix,\nu}}{\sum_\nu T_\nu} \qquad (2.2)$$

I_s is the averaged Intensity as measured by Herschel, whilst $I_{pix,\nu}$ is the image intensity at frequency ν and T_ν is the transmission coefficient at frequency ν.

Repeating this procedure for each band on board SPIRE and PACS allows a dataset of points to be built up as a function of frequency. This dataset then acts as an 'expected' dataset that is described by Equation 1.4. As a direct result of this, fitting Equation 1.4 to the 'expected' dataset using a χ^2 minimisation routine allowed the 2 fit parameters, N and T to be determined.

2.2.2. Parameter estimation

A χ^2 minimisation test is a statistical test to assess the 'goodness-of-fit' between observed data and a theoretical model. The value of χ^2 is determined via Equation 2.2.2 (Taylor 1997).

$$\chi^2 = \sum_i \left(\frac{O_i - E_i}{\sigma_i} \right)^2 \qquad (2.3)$$

O_i is an observed point, and E_i is the expected point. σ_i is the standard deviation of O_i. If O_i is a given dataset and E_i is the model that is expected to fit that dataset, then χ^2 is therefore a measure of how close that model fits the data within one standard deviation.

By applying this χ^2 test to assess how well the modified blackbody given in Equation 1.4 fits the observed data, recovery of both N and T was possible. This was achieved on a pixel by pixel basis. Prior to any parameter estimation it was first necessary to account for the fact that the model being fitted for was continuous across a frequency range ν and not, as the observed points dictated, 6 discrete intensity values. To solve this, the index in the frequency range ν at which each band was located
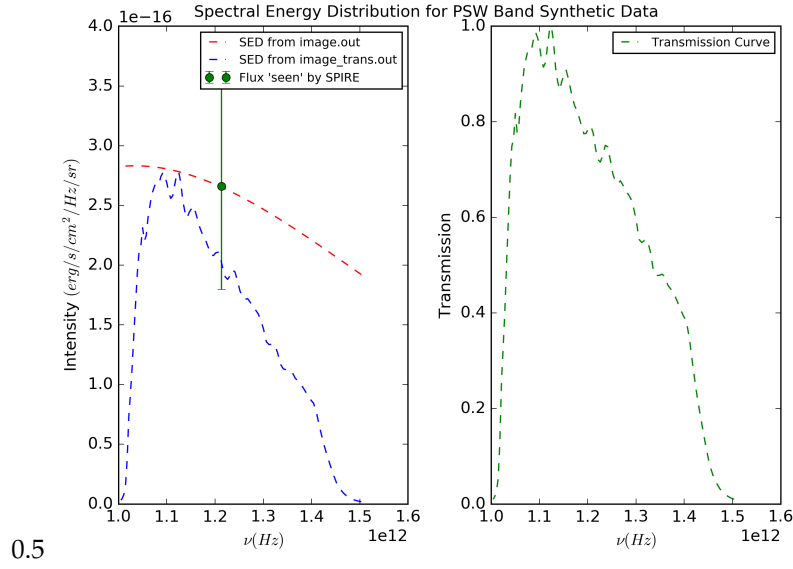
0.5

Figure 2.6: *A figure showing the continuous SED sampled from* `image_trans.out`*, along with the SED after convolving with the transmission curve (right hand panel). Also illustrated is the discrete point that Herschel would see were it to be observe this source in its PSW band.*

$k - \sigma$	P	$M = 1$	$M = 2$	$M = 3$	$M = 4$
$1 - \sigma$	68%	1	**2.30**	3.53	4.72
$2 - \sigma$	95.4%	4	**6.17**	8.02	9.70
$3 - \sigma$	99.73%	9	**11.8**	14.2	16.3

Table 2.1: *A table showing the values of $\Delta\chi^2$ for fit parameters in varying M dimensions. Bold parameters are those used in this study (Press, Flannery, and Teukolsky 1986)*

was found. As the continua produced by the model was evaluated over the same frequency range ν, the index of each band in ν was also the index of the intensity in each band [PROBABLY REQUIRES REWRITING - DIFFICULT TO ARTICULATE]. By then evaluating Equation 1.4 at a given value of N and T the expected datapoints were determined. Subsequently pulling out the points within this curve that match the bands and applying the χ^2 test given in Equation 2.2.2 allowed the 'goodness-of-fit' of that given curve to the observed data to be evaluated. Systematically repeating this process across all values of N and T allowed a χ^2 landscape to be built up. The minimum value of χ^2 within this landscape corresponded to the theoretical best fit; by locating the values of N and T that produced this curve, the best fit parameters were determined. This proecedure was then applied to the next pixel in the image until all pixels had been analysed and their best fit parameters estimated, therefore producing best fit values of N and T at each pixel.

Thi χ^2 fitting routine was also the major source of errors in N and T estimation and so these errors were accounted for accordingly. This was performed by way of analysing the $\Delta\chi^2$ landscape.

By expressing χ^2 as $\chi^2 = \chi^2_{min} + \Delta\chi^2$, a region around $\chi^2_m in$ can be isolated by drawing lines of constant χ^2 characterised by $\Delta\chi^2$. These region contains a varying percentage of the fit parameters depending upon the value of $\Delta\chi^2$ described in Table 2.1.

This project required 2 fit parameters in N and T. The values of $\Delta\chi^2$ used in this study are shown in bold in Table 2.1. The corresponding confidence interval is shown in the P column. All errors quoted hereafter correspond to the $3 - \sigma$ interval.

2.3. Image construction

2.3.1. 2D Maps of N and T

The result of the χ^2 minimisation is a best fit value of N and T at each pixel. By using `matplotlib.pyploy.imshow` these values can be plotted as 2-dimensional heat maps that graphically illustrate the recovered values. This process was also repeated by constructing values of N and T from the initial input data files `dust_density.inp` and `dust_temperature.dat` by Equations 2.3.1 and 2.3.1.

$$N_{col} = \frac{\sum \rho_d V_{los}}{\mu m_p R_{dust-gas}} \frac{1}{D^2 \sigma} \qquad (2.4)$$

$$T_{col} = \frac{\sum_i T_i \rho_i}{\sum_i \rho_i} \qquad (2.5)$$

Within Equation 2.3.1, N_{col} is the column density of the pixel, ρ_d is the dust density at that pixel, V_{los} is the volume of the pixels along the line of sight, μ is the mean molecular weight, m_p is the mass of the proton, $R_{dust-gas}$ is the dust to gas ratio, D is the distance to the source and σ is the solid angle of the pixel.

Within Equation 2.3.1, T_{col} is the temperature of the pixel, T_i and ρ_i are the column-weighted temperature and dust density at ith pixel along the line of sight. This accounts for the fact that temperature inputs to RADMC-3D are column-weighted.

Computing maps of N and T from both the χ^2 recovered values as well as the theoretical predictions based on Equations 2.3.1 and 2.3.1 from the input data allows both data to be compared and constrasted.

Along with maps of N and T, probability density functions (PDFs) were also computed. These allowed the distribution of N and T within a given map to be analysed. It also allowed a further measure of comparison between χ^2 and theoretical predictions.

2.3.2. Dendrogram analysis

As Section 1.1.1 stated, molecular clouds have a hierarchical structure according to their fragmentation and collapse. This produces a complex structure within the cloud, often with regions of having substructure according to any hierarchical fragmentation that it may undergo during collapse. This structure can be analysed using maps of N but it can also be probed with dendrogramic analysis.

A dendrogram is a graphical representation that shows the relationship between individual datapoints in a set by way of a tree diagram. An example dendrogram is shown Figure 2.3.2.

As Figure 2.3.2 shows, the dendrogram highlights the relationships between areas in the image. If Figure 2.3.2 represents an idealised molecular cloud then the fragmented structure represents regions of consecutively greater density. The dendrogram highlights this in a tree diagram format.

The initial vertical line of the dendrogram in Figure 2.3.2 is the trunk: the first representation of structure. From here the dendrogram probes the next level of structure, illustrated by the first vertex. A leaf respresents a structure that has no further substructure, whilst a branch represents an area that has further structure. The 'taller' the dendrogram the greater the number of individual levels of substructure.

The Python software package `astrodendro` was used to produce dendrograms for this project (Robitaille et al. n.d.).
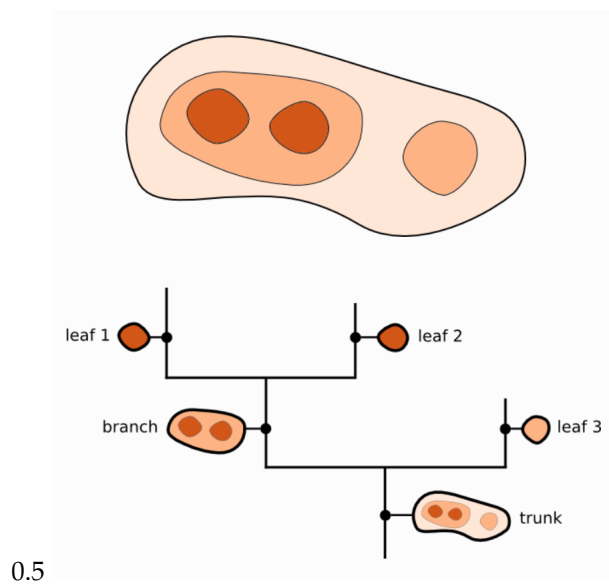
0.5

Figure 2.7: *An idealised molecular cloud containing some substructure defined by sequentially darker regions. Below, the dendrogramic representation of the cloud (astrodendro 2016).*

Chapter 3

Results

Chapter 4

Discussion

Chapter 5

Conclusion

Appendix

All code was version controlled using GitHub and stored in a private repository throughout development. The repository containing all code can be found at http://www.github.com/tomasjames/ZiggyStarDust.

Bibliography

astrodendro (2016). *Astronomical Dendrograms in Python*. [Online; accessed April 21, 2016]. URL: `https://dendrograms.readthedocs.org/en/latest/_images/schematic_structure_1.png`.

Bjorkman J. E. and Wood K. (2001). "Radiative Equilibrium and Temperature Correction in Monte Carlo Radiation Transfer". 554, pp. 615–623. DOI: `10.1086/321336`. eprint: `astro-ph/0103249`.

Caltech. *IRAS Image of Rho Ophiuchi*. File: `rho.jpg`. URL: `http://coolcosmos.ipac.caltech.edu/image_galleries/IRAS/roph.html`.

Dobbs C. L., Burkert A., and Pringle J. E. (2011). "Why are most molecular clouds not gravitationally bound?" 413, pp. 2935–2942. DOI: `10.1111/j.1365-2966.2011.18371.x`. arXiv: `1101.3414`.

Draine B. T. and Lee H. M. (1984). "Optical properties of interstellar graphite and silicate grains". 285, pp. 89–108. DOI: `10.1086/162480`.

Dullemond C., Juhasz A., Pohl A., Sereshti F., Shetty R., Peters T., Commercon B., and Flock M. *RADMC-3D: A multi-purpose radiative transfer tool*. Version 0.38.

Dullemond C., Juhasz A., Pohl A., Sereshti F., Shetty R., Peters T., Commercon B., Flock M., and Min M. *Manual for RADMC-3D*. English. Version Version 0.39. Universität Heidelberg. 174 pp.

ESA. *Herschel Fact Sheet*. Fact-sheet. URL: `http://esamultimedia.esa.int/docs/herschel/Herschel-Factsheet.pdf`.

Garcia-Lario P. et al. *Herschel Observer's Manual*. English. Version Version 5.0.3. ESA. 124 pp.

Griffin M. J. et al. (2010). "The Herschel-SPIRE instrument and its in-flight performance". 518, L3, p. L3. DOI: `10.1051/0004-6361/201014519`. arXiv: `1005.5123 [astro-ph.IM]`.

Helmich F. P. (2011). "Herschel HIFI - the Heterodyne Instrument for the Far-Infrared". *EAS Publications Series*. Ed. by M. Röllig et al. Vol. 52. EAS Publications Series, pp. 15–20. DOI: `10.1051/eas/1152003`.

Hildebrand R. H. (1983). "The Determination of Cloud Masses and Dust Characteristics from Submillimetre Thermal Emission". 24, p. 267.

Jeans J. H. (1902). "The Stability of a Spherical Nebula". *Philosophical Transactions of the Royal Society of London A: Mathematical, Physical and Engineering Sciences* 199.312-320, pp. 1–53. ISSN: 0264-3952. DOI: `10.1098/rsta.1902.0012`. eprint: `http://rsta.royalsocietypublishing.org/content/199/312-320/1.full.pdf`. URL: `http://rsta.royalsocietypublishing.org/content/199/312-320/1`.

Juhasz A. *radmc3dPy*. Version 0.25.

Keene J. et al. (1980). "Far-infrared observations of the globule B335". 240, pp. L43–L46. DOI: `10.1086/183320`.

Kelly B. C. et al. (2012). "Dust Spectral Energy Distributions in the Era of Herschel and Planck: A Hierarchical Bayesian-fitting Technique". 752, 55, p. 55. DOI: `10.1088/0004-637X/752/1/55`. arXiv: `1203.0025 [astro-ph.IM]`.

Krumholz M. R. (2011). "Star Formation in Molecular Clouds". *American Institute of Physics Conference Series*. Ed. by E. Telles, R. Dupke, and D. Lazzaro. Vol. 1386. American Institute of Physics Conference Series, pp. 9–57. DOI: `10.1063/1.3636038`. arXiv: `1101.5172`.

Larson R. B. (1994). "The Structure and Content of Molecular Clouds 25 Years of Molecular Radioastronomy: Proceedings of a Conference Held at Schloss Ringberg, Tegernsee, Germany 14–16 April 1993". Ed. by T. L. Wilson and K. J. Johnston. Berlin, Heidelberg: Springer Berlin Heidelberg. Chap. The evolution of molecular clouds, pp. 13–28. ISBN: 9783540490357. DOI: `10.1007/3540586210_2`. URL: `http://dx.doi.org/10.1007/3540586210_2`.

Mamajek E. E. (2008). "On the distance to the Ophiuchus star-forming region". *Astronomische Nachrichten* 329, p. 10. DOI: `10.1002/asna.200710827`. arXiv: `0709.0505`.

Murphy D. and von Schill L. (2014). "Filamentary Structure in Molecular Clouds". Filaments 2014. URL: `https://science.nrao.edu/science/meetings/2014/filamentary-structure`.

Pettini M. (2011). "Structure and Evolution of Stars". University Lecture.

Poglitsch A. and Altieri B. (2009). "The PACS Instrument". *EAS Publications Series*. Ed. by L. Pagani and M. Gerin. Vol. 34. EAS Publications Series, pp. 43–62. DOI: `10.1051/eas:0934004`.

Press W. H., Flannery B. P., and Teukolsky S. A. (1986). *Numerical recipes. The art of scientific computing*.

Robitaille T. et al. *astrodendro: Python package for computation of astronomical dendrograms*. Version 0.1.0.

Shetty R., Kauffmann J., Schnee S., and Goodman A. A. (2009). "The Effect of Noise on the Dust Temperature-Spectral Index Correlation". 696, pp. 676–680. DOI: `10.1088/0004-637X/696/1/676`. arXiv: `0902.0636 [astro-ph.GA]`.

Shetty R., Kauffmann J., Schnee S., Goodman A. A., and Ercolano B. (2009). "The Effect of Line-of-Sight Temperature Variation and Noise on Dust Continuum Observations". 696, pp. 2234–2251. DOI: `10.1088/0004-637X/696/2/2234`. arXiv: `0902.3477 [astro-ph.GA]`.

SVO Filter Profile Service. *Filer Profile Service: An experiment about filter standardization in the VO*. Online database comprising values and data for filter profiling. URL: `http://svo2.cab.inta-csic.es/svo/theory/fps3/index.php?mode=browse&gname=Herschel&gname2=Pacs`.

Taylor J. (1997). *Introduction to Error Analysis, the Study of Uncertainties in Physical Measurements, 2nd Edition*. University Science Books. Chap. Chapter 12: The Chi-Squared Test of a Distribution.